

## Article

# Thermal Stress Compensation for an Aircraft Engine Duct System Based on a Structural Redesign of Tie Rods

Xinghai Li <sup>1</sup>, Kai Feng <sup>1</sup>, Jie Yuan <sup>2,\*</sup>, Rui Wang <sup>3</sup>, Kaijie Yang <sup>2</sup>, Rentong Zheng <sup>3</sup> and Yansong Wang <sup>2</sup>

- <sup>1</sup> Shenyang Engine Research Institute, Aero Engine Corporation of China (AECC), Shenyang 110015, China; lixinghai\_hf@163.com (X.L.); fengkai\_hf163@163.com (K.F.)
- <sup>2</sup> College of Aerospace Engineering, Nanjing University of Aeronautics & Astronautics, Nanjing 210016, China; yang\_kaijie@nuaa.edu.cn (K.Y.); wys840017707@163.com (Y.W.)
- <sup>3</sup> School of Energy & Power, Jiangsu University of Science and Technology, Zhenjiang 212003, China; wray980801@163.com (R.W.); zhengrt99@163.com (R.Z.)
- \* Correspondence: jieyuan@nuaa.edu.cn

**Abstract:** The reliability of the aircraft engine duct system is of paramount importance as it directly affects the safety of the aircraft, particularly under high-temperature and high-pressure cycles. In this study, ANSYS Workbench was used for finite element analysis, and a sleeve-type tie rod structure was proposed to address the critical problem of tie rod tearing during the operation of the duct system, thereby optimizing thermal stress compensation for the duct system. The research results show the following: (1) The anchor of the traditional tie rod imposes displacement constraints on the thermal deformation of the duct system, leading to stress concentration and even structural failure in the connection area between a duct and a tie rod. (2) The improved sleeve-type tie rod provides greater axial displacement freedom for the duct, effectively mitigating stress concentration phenomena. (3) Taking a worst-case scenario of 537.78 °C and 2 MPa as an example, the sleeve-type tie rod proposed in this paper can reduce the stress at the tie rod connection from 757.61 MPa to less than 25 MPa, a reduction of more than 96%. The original tie rod tearing problem is solved, and the maximum stress of the whole duct system is reduced to 459.25 MPa, which is below the yield strength.



**Citation:** Li, X.; Feng, K.; Yuan, J.; Wang, R.; Yang, K.; Zheng, R.; Wang, Y. Thermal Stress Compensation for an Aircraft Engine Duct System Based on a Structural Redesign of Tie Rods. *Appl. Sci.* **2023**, *13*, 9519. <https://doi.org/10.3390/app13179519>

Academic Editor: Satoru Okamoto

Received: 21 June 2023

Revised: 12 August 2023

Accepted: 16 August 2023

Published: 22 August 2023



**Copyright:** © 2023 by the authors. Licensee MDPI, Basel, Switzerland. This article is an open access article distributed under the terms and conditions of the Creative Commons Attribution (CC BY) license (<https://creativecommons.org/licenses/by/4.0/>).

**Keywords:** engine duct; stress analysis; high temperature and pressure; tie rods; finite element

## 1. Introduction

The air duct system of an aircraft engine serves as a vital component responsible for extracting air from the engine and supplying high-temperature and high-pressure air to downstream subsystems. Situated closely on the engine's surface, it is often referred to as the "blood vessels" of the aircraft engine. The design of the air duct system for safety and reliability not only influences the functionality of the air supply but also significantly impacts the safety of the engine itself and the surrounding equipment. Hence, the design of the engine air duct system assumes paramount importance. Due to the flow of high-temperature and pneumatic gas through the engine air duct system, thermal deformation of the ducts may occur. To prevent interference with the surrounding equipment resulting from deformed ducts, two methods, namely tie rods and guides, are commonly employed to support or constrain the engine ducts. Among these methods, tie rods find wider application due to their ease of installation and fewer spatial limitations. However, the welded connection between the tie rod and the duct can lead to local stress concentration and even tie rod fracture when the duct experiences significant thermal deformation, posing severe challenges to the reliability of the engine duct system.

Currently, stress distribution analysis methods for tie rod structures predominantly comprise theoretical analysis, experimental exploration, and finite element simulation. Theoretical analysis and experimental inquiry methods [1–4], due to their constraints in

practical situations, have limited application. Consequently, the simulation of models using finite element software is the most widely employed approach. Additionally, tie rod reliability has been extensively analyzed using the finite element method by numerous researchers [5–12]. Liu et al. [13] studied the rotor tie rod stress distribution and maximum stress location and further optimized the tie rod structure. Xu et al. [14] investigated the effect of the detuning rate of the tie rod, the number of tie rods, etc., on the natural frequency, which provides a reference for the study of the natural frequency of the duct. Brennan et al. [15] studied the longitudinal vibration of large tie rods and proposed that the use of a pneumatic vibration absorber could effectively attenuate the longitudinal vibration. Duan et al. [16,17] studied the structural behavior of two types of steel tie rod threaded connections using finite element analysis in ANSYS and presented the equivalent force distribution, interface contact pressure, and sliding distance under different axial loads. At the same time, they studied the connection of the thread of the steel tie rod and found the most suitable thread structure through their test. Kim et al. [18] discovered that tie rod buckling is the most severe load condition in the design of tie rod structures. Waybase et al. [19] found that vibration and fatigue failure were the main causes of tie rod failure. Godase et al. [20] and Du et al. [21] pointed out that the strength of tie rods is mainly influenced by bending, tension, load, and shear, among which the shear resistance of tie rods is often neglected. And Godase et al. found that the geometric parameters of the tie rod, such as its outer diameter and inner diameter, have a significant effect on shear stress. Muhammad et al. [22] suggested that the design of the connecting rod should utilize a material with a high strength value and reduced weight to meet the requirements for a stronger connecting rod. Bhirad [23] found that the material and diameter of the tie rod had a great influence on the failure of the tie rod. Furthermore, he also carried out stress analysis on the shape of the tie rod and concluded that a tie rod with square and circular sections is more complex than a tie rod with only a circular shape. Kim et al. [24], Navale et al. [25], and Wayal et al. [26] found that aluminum tie rods were superior to traditional cast-iron tie rods. Kim et al. also optimized the shape of aluminum tie rods using the RSM and Kriging interpolation method.

Although some theoretical basis and engineering design experience for the fatigue characteristics and optimal arrangement of tie rods have been provided by the aforementioned studies, it should be noted that the majority of these studies were conducted in the civil industry and may not be fully applicable to the investigation of high-temperature duct tie rods in aero-engines. Particularly, the exploration of the coupling between the degrees of freedom of tie rods and the strength of a duct system is lacking [27,28].

In this paper, firstly, finite element analysis is conducted on existing aero-engine tie rods to investigate their behavior under different temperatures. Subsequently, a new structure suitable for aero-engine duct tie rods is proposed with the objective of addressing the issue of potential tie rod fractures that may occur due to significant thermal deformation during high-temperature and high-pressure cycles in an engine duct system. Furthermore, stress calibration of the aforementioned structure is performed, and its reliability and excellence are subsequently verified. Exploring new designs and improvement solutions for aircraft engine duct tie rods leads to opportunities to reduce the stress concentration area, improve the fatigue life of the system, and ultimately enhance the overall performance and efficiency of the aircraft engine duct system.

## 2. Model of the Engine Duct System

### 2.1. Establishment of the Duct System Model

The structure of a certain engine air duct system is shown in Figure 1. The system has a multi-bend spatial layout and a semi-spherical envelope shape overall, including nine bends of different sizes, one reducing duct, one tee tube, three ball joints, two valves, and one tie rod. Among them, the ball joints mainly play a role in temperature compensation, and the tie rod is mainly used for weight support and displacement restraint of the duct.

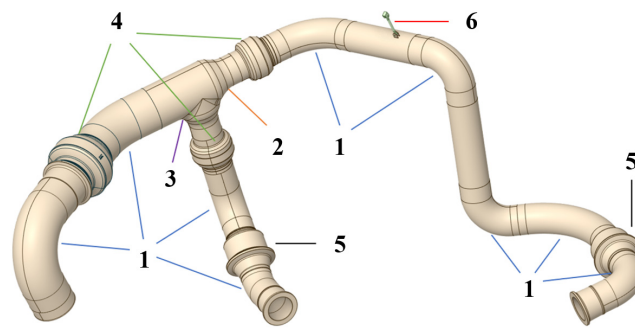


**Figure 1.** Structure diagram of engine air duct system: 1. bends; 2. reducing duct; 3. tee tube; 4. ball joints; 5. valves; 6. tie rod.

Due to the complex structure and large number of components in the air duct system of the engine studied in this paper, it was difficult to establish solid models for all components when building the model of the duct system. Therefore, in stress analysis of the duct system, the effects of certain components on the system can be reflected by simulating their functions. The simplified finite element model of the duct system is shown in Figure 2.

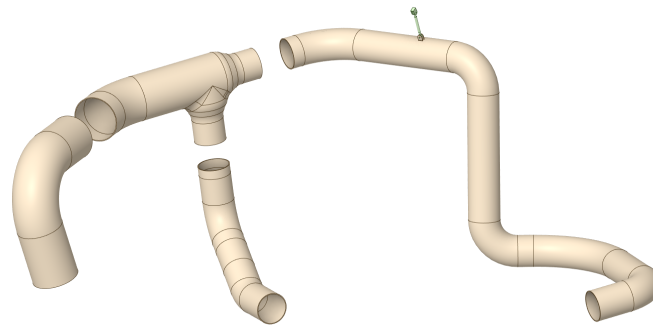


**Figure 2.** Simplified finite element model.

### 2.2. The Fixed End

Figure 3 shows the model of the fixed end of the duct system and the functional implementation diagram.

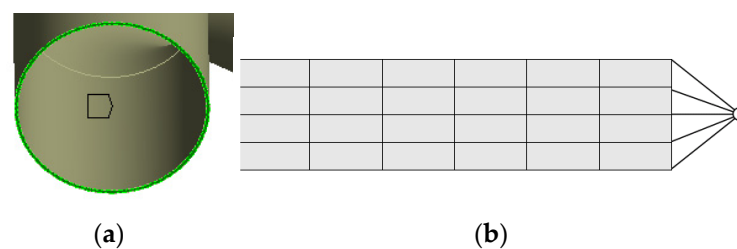


**Figure 3.** Fixed constraint model establishment: (a) structure diagram of fixed end; (b) schematic diagram of fixed end constraint.

As shown in Figure 3, in the finite element simulation calculations, the technique of multi-point constraint and remote control are used to reflect the constraint relationship at the fixed end.

### 2.3. Tie Rod

Figure 4 shows a schematic diagram of the structure of the tie rod used in the aircraft duct system.

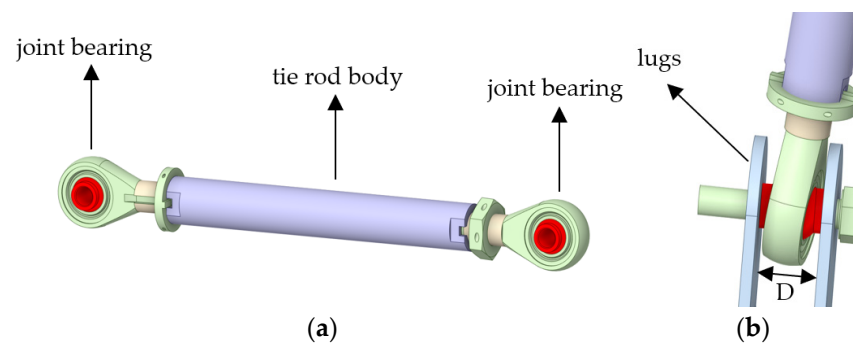


**Figure 4.** Structure diagram of tie rod: (a) model diagram of tie rod; (b) diagram of joint bearing deflection.

As shown in Figure 4a, the tie rod comprises the tie rod body and two end joint bearings, which are shown in Figure 4b. The tie rod is equipped with spherical sliding bearings as joint bearings, which can maintain three rotational degrees of freedom for the tie rod body even after it is fixed to the tie rod lugs, thus ensuring the overall freedom of the tie rod system. Table 1 shows the rotational characteristics of the joint bearings.

**Table 1.** Rotational characteristics of joint bearings.

Direction	Translation Tx	Translation Ty	Translation Tz	Rotation Rx	Rotation Ry	Rotation Rz
Freedom	stiffness	stiffness	stiffness	0–5°	arbitrary	0–5°

According to Table 1, the deflection angle of the tie rod is restricted by the distance  $D$  between the tie rod lugs. The larger the distance between the lugs, the greater the angle that the joint bearing can deflect. The tie rod used in this paper has rotational freedom of 0–5° in the XOY and YOZ planes and unrestricted rotation in the XOZ plane. During actual installation, the tie rod lugs at both ends must be arranged vertically, as shown in Figure 5.

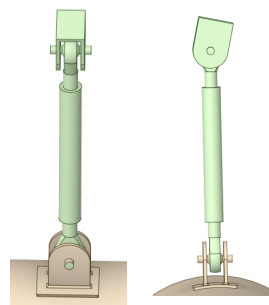


**Figure 5.** Diagram of tie rod lug.

As shown in Figure 5, the connection between the tie rod and the duct system mainly adopts the method of a six-degree-of-freedom constraint connection through welding the tie rod lug base and the duct system surface.

The spherical sliding bearing of the tie rod was implemented using the “Ball Joint” in Workbench, and the modeling schematic is shown in Figure 6.

As shown in Figure 6, the displacement degrees of freedom of the spherical bearings can be constrained by the “Ball Joint” element, while other degrees of freedom are released.

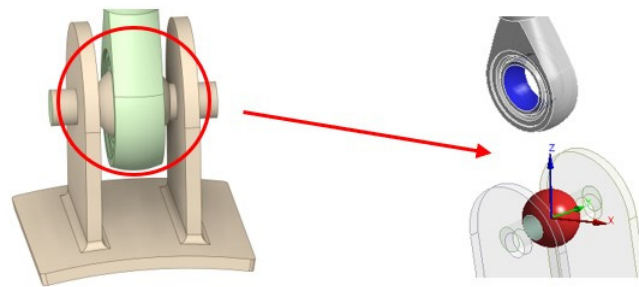


**Figure 6.** Tie rod spherical bearing finite element model.

#### 2.4. Ball Joint

The ball joint is a metallic element used for thermal compensation and increased flexibility in air duct systems. As shown in Figure 7, the ball joint consists primarily of bellows, a guide, and a restrictor. Under the action of the bending moment, this component has lateral rotational freedom with a maximum deflection angle of  $5^\circ$ , no freedom of torsion, and flat motion.

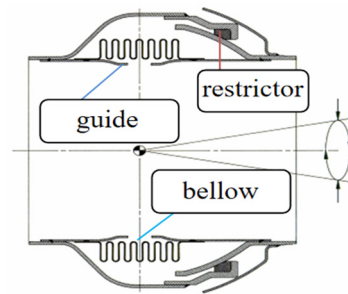


**Figure 7.** Ball joint cross-section.

The ball joint was mainly simulated in Workbench by restricting the degrees of freedom of movement of the ball joint. The model and schematic diagram are shown in Figure 8.

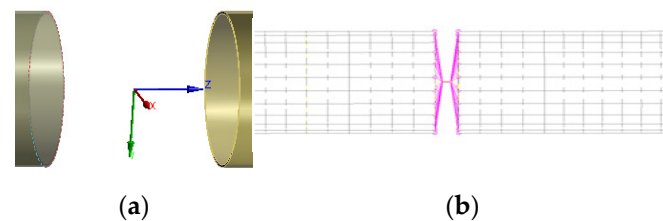


**Figure 8.** Ball joint model establishment: (a) model diagram of ball joint; (b) principle diagram of ball joint constraint.

### 3. Numerical Simulation

#### 3.1. Mesh

In this paper, the ANSYS Mesh module was adopted to generate the mesh, and the mesh is tetrahedral. Before conducting numerical simulations, mesh independence verification was performed on the model. The initial target mesh nodes were 119 thousand, 166 thousand, 207 thousand, 325 thousand, and 481 thousand. Figure 9 shows the results for different mesh sizes. Stress at the lug connection tended to stabilize when the nodes exceeded 207 thousand, and there was no significant change in the results with increasing mesh size. Therefore, considering the mesh density and computer performance, in this paper, the nodes were set to 207,003.

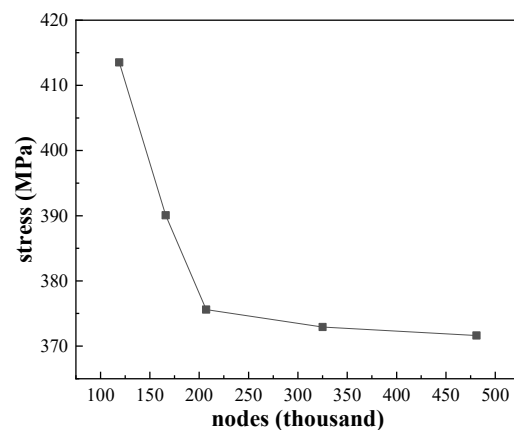


**Figure 9.** Mesh independence verification.

### 3.2. Material Properties

The duct material is a high-temperature alloy (Inconel 625 manufactured by Shanghai Monel Special Alloy Co., Ltd., Shanghai, China), and its material properties are shown in Table 2 [29,30].

**Table 2.** Material properties of Inconel 625.

Temperature (°C)	Yield Strength (MPa)	Young's Modulus (MPa)	Poisson's Ratio	Thermal Expansion Coefficient ( $\times 10^{-6}/^{\circ}\text{C}$ )	Density ( $\text{kg}/\text{m}^3$ )
21.11	655.0	205,471	0.28	12.744	8442.37
37.78	654.8	199,955	0.28	12.751	8442.37
93.33	653.8	190,992	0.28	12.751	8442.37
148.89	652.2	183,407	0.2817	12.830	8442.37
204.44	649.7	179,960	0.2842	12.971	8442.37
260.00	645.8	176,512	0.2864	13.111	8442.37
315.56	639.8	173,754	0.289	13.284	8442.37
371.11	630.5	171,686	0.2922	13.471	8442.37
426.67	616.4	170,307	0.2956	13.660	8442.37
482.22	595.4	168,238	0.2998	13.846	8442.37
537.78	565.1	166,859	0.3049	14.065	8442.37

### 3.3. Boundary Condition

Considering the material parameters and the actual operating conditions within the aircraft envelope, 315.56 °C, 426.67 °C, and 537.78 °C were chosen as the characteristic temperatures for the calculations in this paper. In addition, the duct characteristics at 537.78 °C and duct internal pressures of 1 MPa, 1.5 MPa, and 2 MPa were investigated.

### 3.4. Numerical Calculation

#### 3.4.1. Research Methods

Since the above-established model involves elastic–plastic deformation and contact problems, Static Structural and its built-in Newton–Raphson method [31–37] were used to calculate the von Mises stress of the duct system [38–43], and stress calculation results were obtained under the characteristic operating conditions of the duct system [44].

#### 3.4.2. Variable Temperature Conditions

With the gauge pressure at 0 Pa in the duct, the stress distribution contours of the duct system at various characteristic temperatures are shown in Figures 10–12.

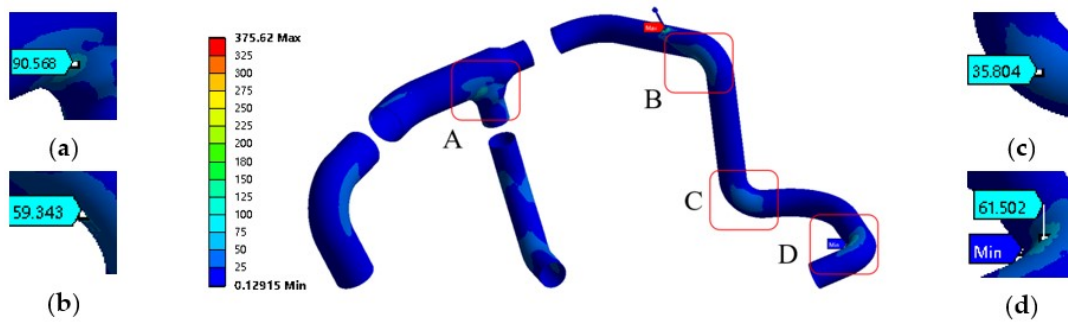


Figure 10. Duct stress distribution at 315.56 °C: (a) region A; (b) region B; (c) region C; (d) region D.

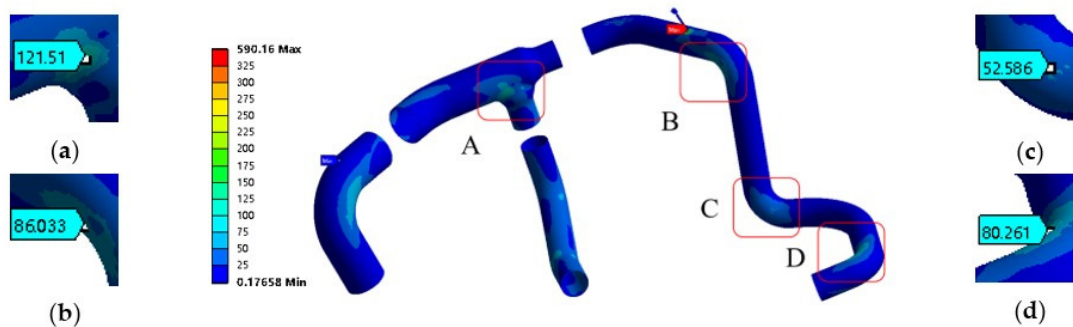


Figure 11. Duct stress distribution at 426.67 °C: (a) region A; (b) region B; (c) region C; (d) region D.

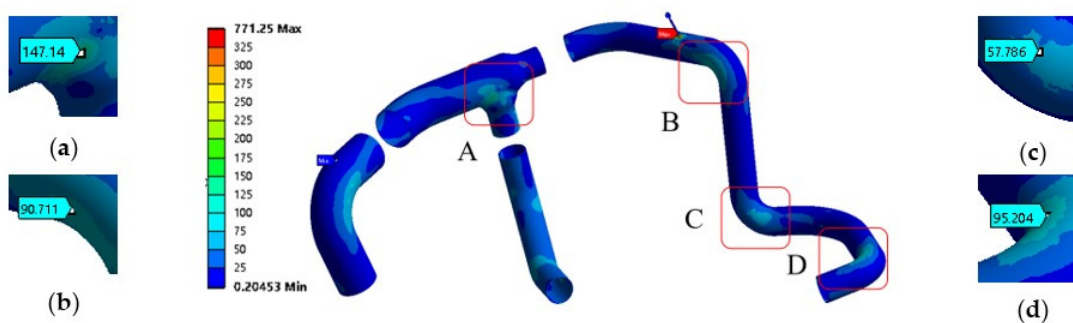


Figure 12. Duct stress distribution at 537.78 °C: (a) region A; (b) region B; (c) region C; (d) region D.

According to Figure 10, under atmospheric pressure conditions, stress concentration was observed at the tees and bends of the duct system due to the high temperature. The main reason for the phenomenon mentioned above is the thermal expansion deformation of the duct, and the internal force distribution was more concentrated in the locations where the spatial curvature or gradient of the tees and bends had changed noticeably. The thermal expansion displacement caused by a high temperature promoted the expansion deformation of the entire annular duct system towards the outer side of the envelope surface. Meanwhile, since the tee is located in the middle of the duct system, the effects produced by the three branches were superimposed, leading to a very obvious concentration of secondary stress. Moreover, as shown in Figures 10–12 with the temperature changing from 315.56 °C to 537.78 °C, the stress concentration phenomenon became more prominent at the position of structural discontinuity, and the maximum stress increase occurred in the tee area of region A at 56.572 MPa.

Furthermore, it is noteworthy that the stress at the connection between the tie rod lug and the duct system increased significantly with temperature variation, as shown in Figure 13.

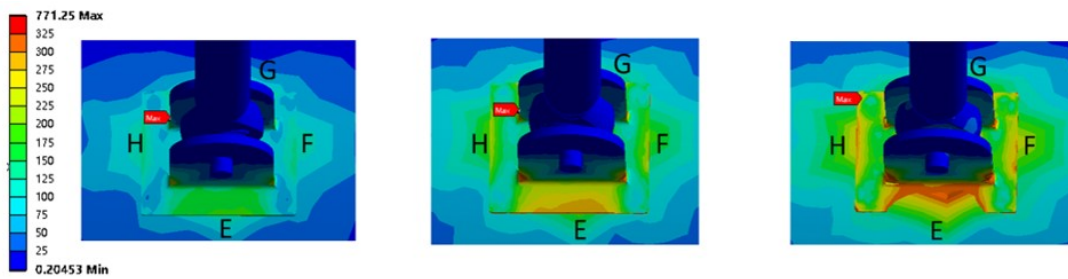


Figure 13. Stress distribution at the lug connection.

According to Figure 13, the stress at points E and G on the tie rod lug base was significantly higher than that at points F and H, and the main reason for this phenomenon is the rotational movement trend of the tie rod lug base around the FH axis, which caused a squeezed state at point E and a stretched state at point H. The maximum stress of the base increased from 375.62 MPa to 771.25 MPa, with an increase of 395.63 MPa, which exceeded the yield limit of 565.1 MPa at this temperature. Specifically, at a temperature of 537.78 °C, the stress in the duct system not only exceeded the limit but also caused separation and failure of the structure.

### 3.4.3. Variable Pressure Conditions

At a constant temperature of 537.78 °C, the stress distribution contours of the duct system under various characteristic pressures are shown in Figures 14–16.

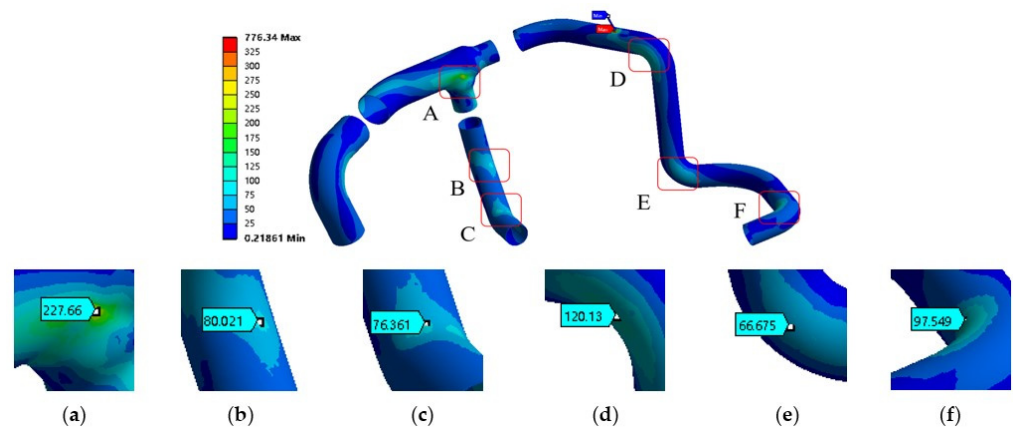


Figure 14. Duct stress distribution at a pressure of 1 MPa: (a) region A; (b) region B; (c) region C; (d) region D; (e) region E; (f) region F.

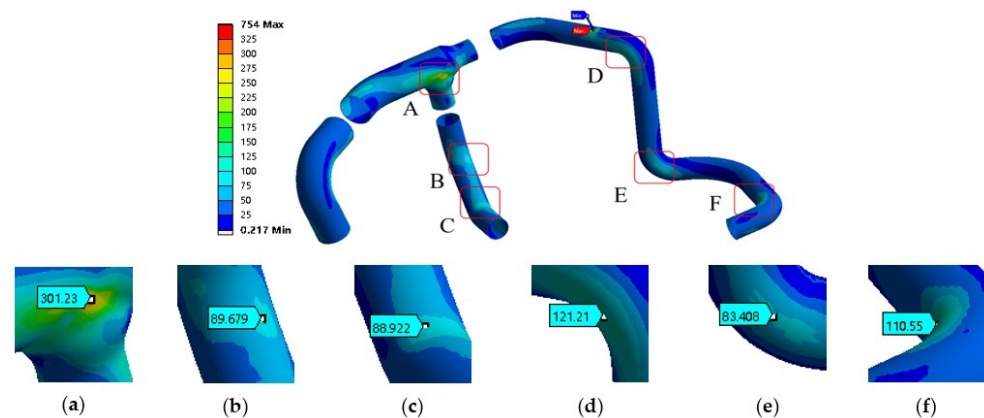
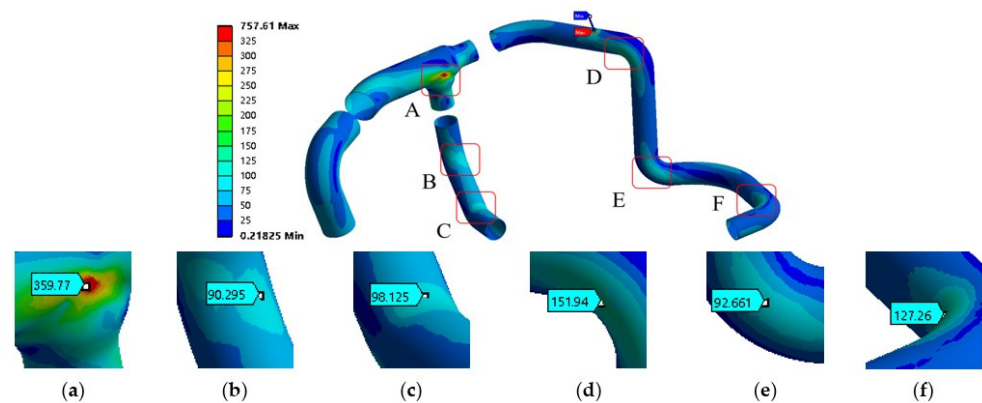


Figure 15. Duct stress distribution at a pressure of 1.5 MPa: (a) region A; (b) region B; (c) region C; (d) region D; (e) region E; (f) region F.



**Figure 16.** Duct stress distribution at a pressure of 2 MPa: (a) region A; (b) region B; (c) region C; (d) region D; (e) region E; (f) region F.

It can be seen from Figures 14–16 that the stress distribution of the duct system is consistent with that in Section 3.4.2. As the pressure increased from 1 MPa to 2 MPa, the maximum stress at the tee joint increased from 227.66 MPa to 359.77 MPa, with an increase of 132.11 MPa. The stress concentration in this region was the most prominent, and the maximum value appeared at the intersection of the tee joint axis due to the more severe superposition of the outward expansion deformation at the tee joint after pressurization.

Furthermore, the stress at the connection between the tie rod lug and the duct system increased overall, as shown in Figure 17.

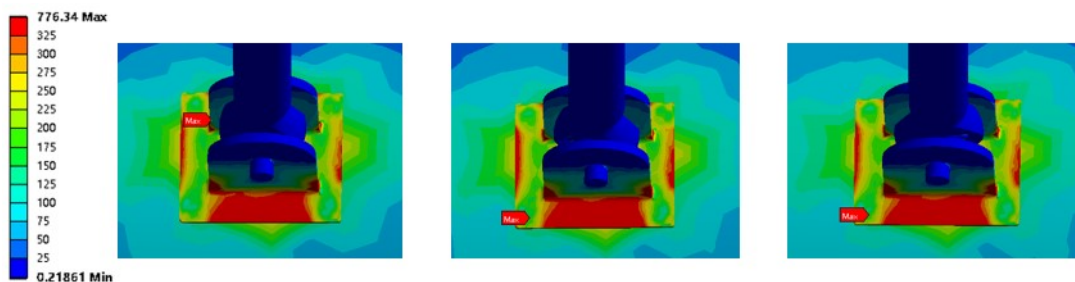


**Figure 17.** Stress distribution at tie rod lug connection.

According to Figure 17, the overall stress of the base increased significantly after pressurization. The stress not only concentrated at the weld points on both sides of the tie rod lug but also spread to the entire base, causing a large increase in stress on both sides of the base in the direction of the duct path. The area where stress exceeded 325 MPa reached half of the base. As the pressure increased from 1 MPa to 2 MPa, the maximum stress fluctuated between 754 MPa and 776.34 MPa. This is because the pressure did not directly act on the base, but it still exceeded the yield limit of 565.1 MPa. It is worth noting that the separation failure phenomenon of the base was alleviated because the duct expanded after pressurization, further fitting the contact surface of the base.

## 4. Redesign

### 4.1. Redesign Solution

Due to the excessive constraint caused by the direct welding of the tie rod base, a sleeve-type tie rod structure is proposed in this paper. The tie rod base is installed on a set of ducts, and there is a gap between the sleeve and the original duct. The model is shown in Figure 18.

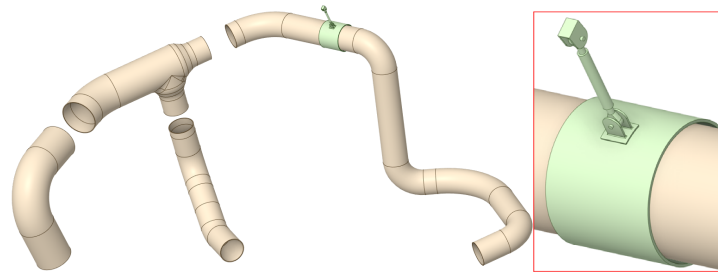


Figure 18. Schematic diagram of optimized design.

According to Figure 18, the proposed solution preserves the space between the sleeve and the duct, but the sleeve does not change the main direction of the external force acting on the duct when the duct undergoes axial deformation during operation. This avoids stress concentration at the tie rod lug base and prevents stress distortion in the duct caused by changes in force. Since the connection method is no longer welding, the additional load on the sleeve is borne by the tie rod itself and does not have a significant impact on the duct. At the same time, it can also reduce the natural frequency of the duct [45].

4.2. Results and Discussion

4.2.1. Variable Temperature Conditions

With the gauge pressure at 0 Pa in the duct, the stress distribution contours of the duct system at various characteristic temperatures are shown in Figures 19–21.

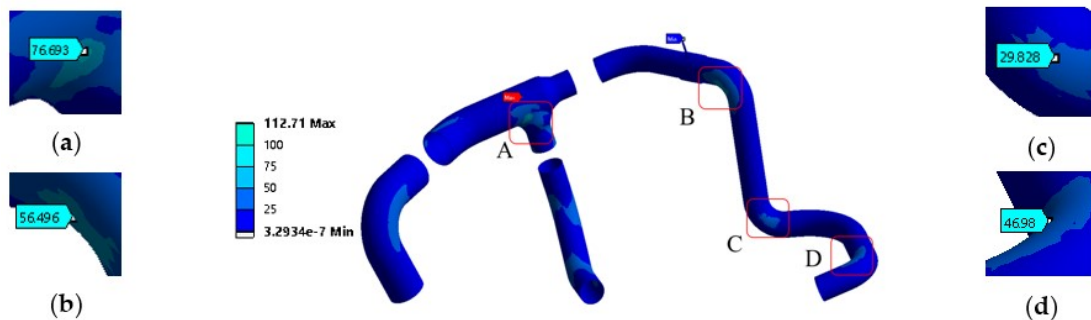


Figure 19. Duct stress distribution at 315.56 °C: (a) region A; (b) region B; (c) region C; (d) region D.

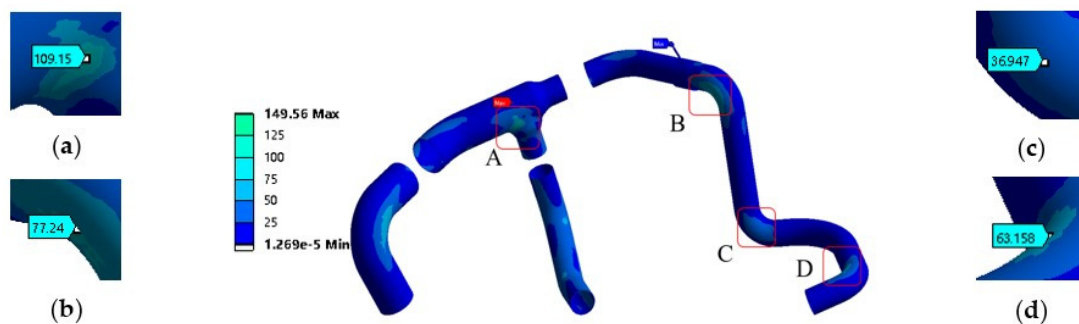


Figure 20. Duct stress distribution at 426.67 °C: (a) region A; (b) region B; (c) region C; (d) region D.

The stress concentration phenomenon in the duct system is noticeably improved by using the sleeve-type tie rod structure, as shown in Figures 19–21. The maximum stress at the temperature of 537.78 °C was reduced to 1.36 MPa, and the overall stress of the tie rod and sleeve was also reduced to below 25 MPa. However, the stress concentration in region B increased slightly after the flexibility of the duct segment at the connection was improved, reaching 86.321 MPa at 537.78 °C. After optimization, the stress in the duct

system at various characteristic temperatures is in accordance with the design requirements. The original problem of structural separation and failure has also been solved.

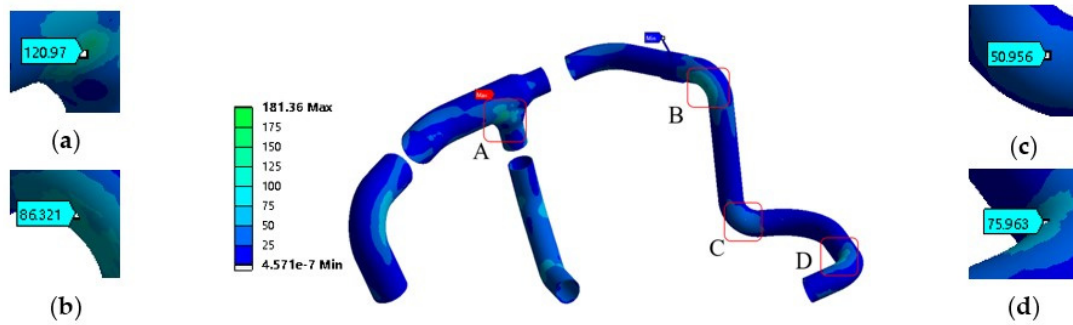


Figure 21. Duct stress distribution at 537.78 °C: (a) region A; (b) region B; (c) region C; (d) region D.

#### 4.2.2. Variable Pressure Conditions

At a constant temperature of 537.78 °C, the stress distribution contours of the duct system under various characteristic pressures are shown in Figures 22–24.

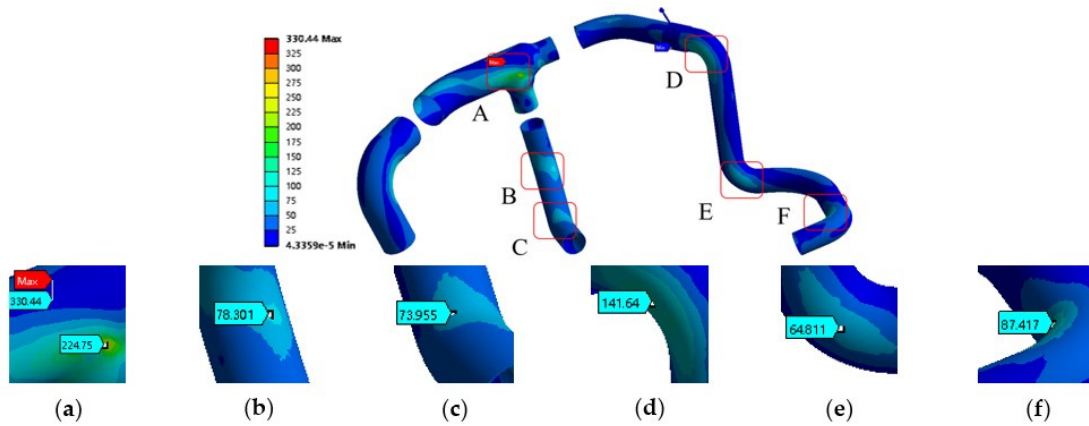


Figure 22. Duct stress distribution at a pressure of 1 MPa: (a) region A; (b) region B; (c) region C; (d) region D; (e) region E; (f) region F.

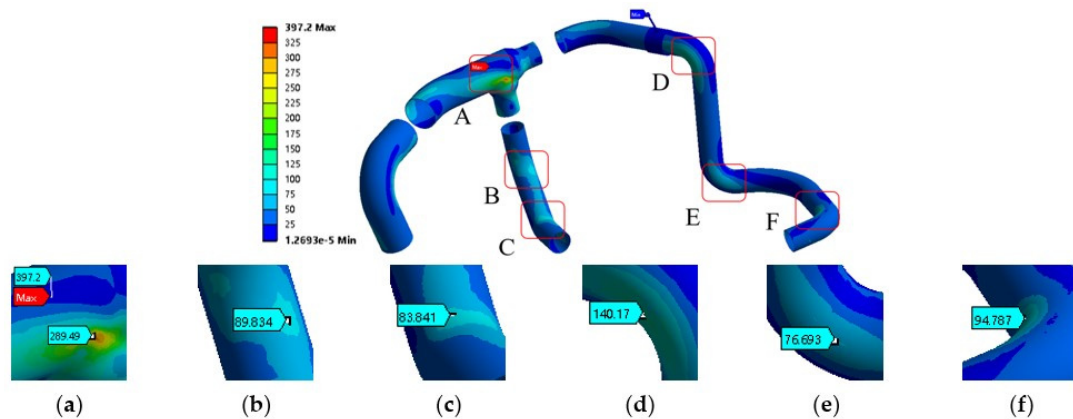


Figure 23. Duct stress distribution at a pressure of 1.5 MPa: (a) region A; (b) region B; (c) region C; (d) region D; (e) region E; (f) region F.

As illustrated in Figures 22–24, no notable alterations were observed in the stress distribution of the duct system following pressurization; however, there was a shift in the location of the maximum stress point towards the outer region of the tee envelope. With an

increase in pressure from 1 MPa to 2 MPa, the maximum stress rose from 330.44 MPa to 459.25 MPa. Nevertheless, it should be noted that the stress levels within the duct system still comply with the design requirements. It is worth noting that the stress of the duct system is more influenced by temperature rather than pressure.

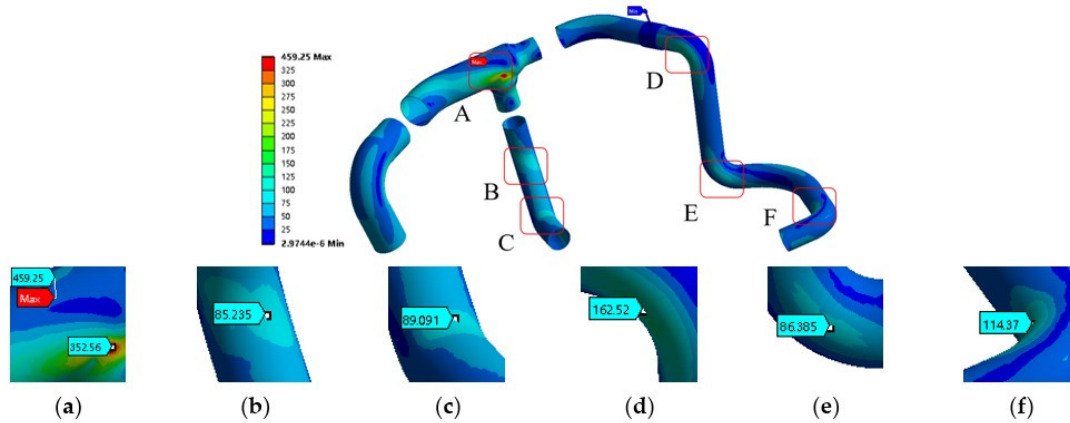


Figure 24. Duct stress distribution at a pressure of 2 MPa: (a) region A; (b) region B; (c) region C; (d) region D; (e) region E; (f) region F.

4.3. Comparison and Analysis

As shown in Figures 25 and 26, further quantitative comparative analysis was performed on regions A, B, C, and D.

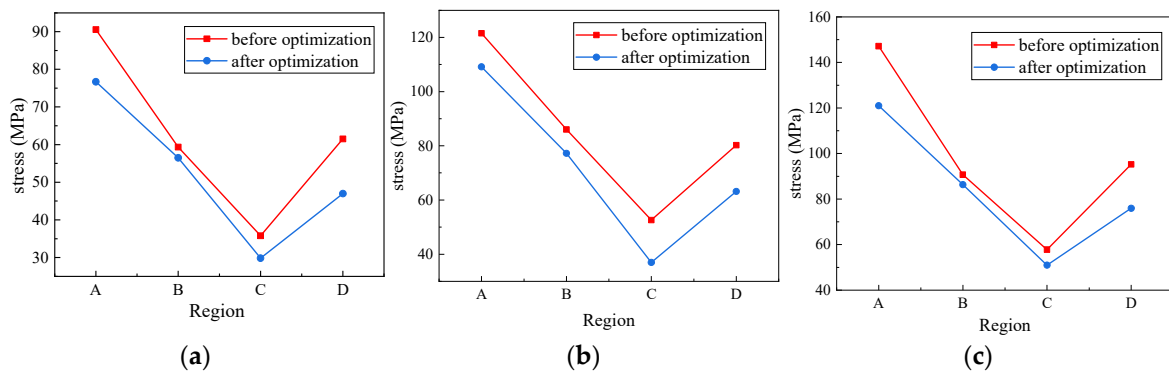


Figure 25. Comparison of stress under constant pressure conditions: (a) 315.56 °C; (b) 426.67 °C; (c) 537.78 °C.

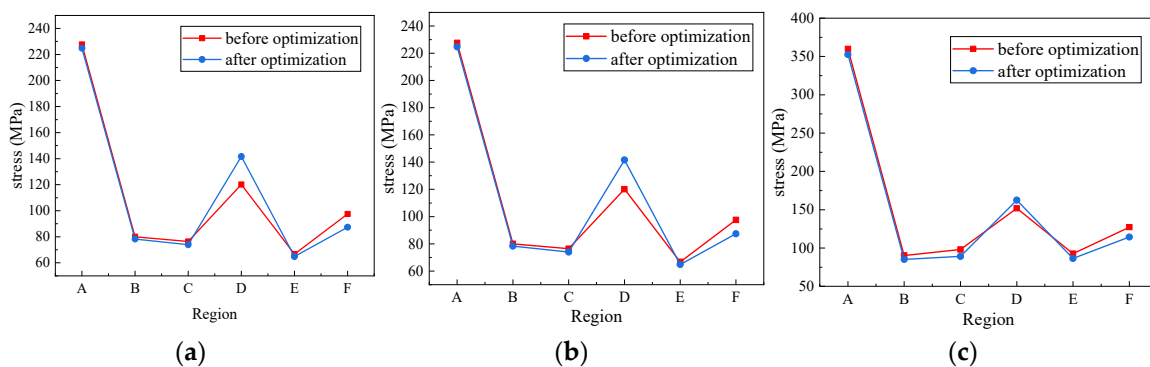


Figure 26. Comparison of stress under thermostatic conditions: (a) 1 MPa; (b) 1.5 MPa; (c) 2 MPa.

As shown in Figures 25 and 26, the effect of temperature on the stresses in the duct system is greater than the effect of pressure on the stresses in the duct system. It is

noteworthy that the self-compensation phenomenon of the bend structure in region D under variable pressure conditions is more noticeable because the alterations of the tie rod connections make the duct system more flexible. Although the local stress in this region rose by about 13%, it was always much less than the yield limit of 565.1 MPa. The obtained research results highlight the significant stress relief capability of the proposed sleeve-type tie rod for the duct system. Particularly, the change in the tie rod connection method effectively diminishes the stress exerted on the original tie rod contact surface while enhancing stress distribution in various areas, such as bends and tees, across the entire duct system.

## 5. Conclusions

As a critical component of the duct system, the tie rod plays a vital role in ensuring the safety and reliability of the overall system. In this paper, thermal stress analysis of a specific engine duct system was conducted using the finite element method in an attempt to investigate the impact of temperature and pressure on the stress characteristics of the duct system. Based on these findings, a sleeve-type tie rod connection structure was proposed, and its influence on the stress characteristics of the duct system was thoroughly analyzed and validated. The following conclusions were finally obtained:

- (1) Under atmospheric pressure conditions, as the temperature increased from 315.56 °C to 537.78 °C, the maximum stress of the duct system increased from 375.62 MPa to 771.25 MPa. When the temperature was maintained at 537.78 °C, the maximum stress of the duct system fluctuated between 754 MPa and 776.34 MPa as the pressure changed from 1 MPa to 2 MPa. The stress of the duct system varied significantly with temperature.
- (2) Owing to the limited rotational freedom of the conventional spherical bearing at the tie rod end, a high level of restraint exists between the tie rod and the duct system, particularly at their contact position. In the case of the investigated air duct system, when the temperature reached 426.67 °C, the stress reached 590.61 MPa, which exceeded the yield limit of 565.1 MPa. However, the high temperature experienced in the engine air duct system often exceeds this limit, and the duct stress will be worse when high pressure is exerted.
- (3) The problem of limited tie rod freedom is effectively addressed by the proposed sleeve-type tie rod as it allows for the release of axial displacement of the duct system at the tie rod position. Particularly during instances of significant deformation in high-temperature ducts, it can mitigate the additional force exerted by the tie rod on the duct system. Under the worst-case scenario of 537.78 °C and 2 MPa as an example, the sleeve-type tie rod proposed in this paper can reduce the stress at the tie rod connection from 757.61 MPa to less than 25 MPa, a reduction of more than 96%. The original tie rod tearing problem is solved, and the maximum stress of the whole duct system is reduced to 459.25 MPa, which is below the yield strength. Expanding the degrees of freedom while avoiding excessive constraints remains the best strategy for mitigating thermal stresses, and this principle is equally applicable in all cases.

**Author Contributions:** Conceptualization, X.L. and K.F.; methodology, X.L. and Y.W.; software, J.Y.; validation, R.W., K.Y. and R.Z.; formal analysis, Y.W.; investigation, K.Y.; resources, X.L.; data curation, K.F.; writing—original draft preparation, R.W.; writing—review and editing, J.Y.; visualization, R.Z.; supervision, X.L.; project administration, K.F.; funding acquisition, J.Y. All authors have read and agreed to the published version of the manuscript.

**Funding:** This research was supported by the Research Fund of Key Laboratory of Aircraft Environment Control and Life Support, MII, Nanjing University of Aeronautics and Astronautics (Grant No. KLAECLS-E-202201).

**Institutional Review Board Statement:** Not applicable.

**Informed Consent Statement:** Not applicable.

**Data Availability Statement:** The data used to support the findings of this study are available from the corresponding author upon request.

**Conflicts of Interest:** The authors declare no conflict of interest.

## References

1. Xu, H.; Yang, L.; Xu, T. Dynamic Analysis of the Rod-Fastened Rotor Considering the Characteristics of Circumferential Tie Rods. *Appl. Sci.* **2021**, *11*, 3829. [\[CrossRef\]](#)
2. Kai, C.; Xu, J. Mechanical Properties of Sheet Pile Cofferdam during Adjacent Open Cut Tunnel Construction near Lake Bottom. *Appl. Sci.* **2023**, *13*, 6191. [\[CrossRef\]](#)
3. Camassa, D.; Castellano, A.; Fraddosio, A.; Miglionico, G.; Piccioni, M.D. Dynamic Identification of Tensile Force in Tie-Rods by Interferometric Radar Measurements. *Appl. Sci.* **2021**, *11*, 3687. [\[CrossRef\]](#)
4. Duvnjak, I.; Ereiz, S.; Damjanović, D.; Bartolac, M. Determination of Axial Force in Tie Rods of Historical Buildings Using the Model-Updating Technique. *Appl. Sci.* **2020**, *10*, 6036. [\[CrossRef\]](#)
5. Shi, H. Study on Safety Design and Leakage Detection Technology of the Aircraft Pneumatic Duct System. Ph.D. Thesis, Nanjing University of Aeronautics and Astronautics, Nanjing, China, 2013.
6. Winklberger, M.; Heftberger, P.; Sattlecker, M.; Schagerl, M. Fatigue strength and weight optimization of threaded connections in tie-rods for aircraft structures. *Procedia Eng.* **2018**, *213*, 374–382. [\[CrossRef\]](#)
7. Tang, M.; Wang, Q.; He, G.; Liu, R.P. Based on Bionic Optimization Design and Strength Analysis of The Tie Rod of Aircraft Landing Gear. *IOP Conf. Ser. Mater. Sci. Eng.* **2020**, *816*, 012007. [\[CrossRef\]](#)
8. Falco, A.D.; Resta, C.; Sevieri, G. Sensitivity analysis of frequency-based tie-rod axial load evaluation methods. *Eng. Struct.* **2021**, *229*, 111568. [\[CrossRef\]](#)
9. Ereiz, S.; Duvnjak, I.; Damjanović, D.; Bartolac, M. Analysis of Seismic Action on the Tie Rod System in Historic Buildings Using Finite Element Model Updating. *Buildings* **2021**, *11*, 453. [\[CrossRef\]](#)
10. Dai, X.; Feng, S.; Zhu, J.; Tian, J.; Zhou, J.; Yu, L. Analysis of Assembly Deformation of a Detachable High Speed Rotor Tie Rod. In Proceedings of the 2021 IEEE International Conference on Mechatronics and Automation (ICMA), Takamatsu, Kagawa, Japan, 8 August 2021. [\[CrossRef\]](#)
11. Kim, J.K.; Kim, Y.J.; Yang, W.H.; Park, Y.C.; Lee, K. Structural design of an outer tie rod for a passenger car. *Int. J. Auto. Tech-KOR* **2011**, *12*, 375–381. [\[CrossRef\]](#)
12. Mungi, S.; Navthar, R.R. Performance Optimization of Tie rod using FEA. *Int. J. Eng. Res. Dev.* **2015**, *11*, 27–33.
13. Liu, X.; Yuan, Q.; Ou, W.H. Strength Analysis and Design Improvement of the Tie Rods in Circumferentially Distributed Rod Fastening Rotors. *J. Xi'an Jiaotong Univ.* **2016**, *50*, 104–110. [\[CrossRef\]](#)
14. Xu, H.; Yang, L.; Xu, T.; Wu, Y. Effect of Detuning of Clamping Force of Tie Rods on Dynamic Performance of Rod-Fastened Jeffcott Rotor. *Math. Probl. Eng.* **2021**, *2021*, 6645978. [\[CrossRef\]](#)
15. Brennan, M.J.; Day, M.J.; Randall, R.J. An Experimental Investigation into the Semi-Active and Active Control of Longitudinal Vibrations in a Large Tie-Rod Structure. *J. Vib. Acoust.* **1998**, *120*, 1–12. [\[CrossRef\]](#)
16. Duan, W.; Joshi, S. Structural behavior of large-scale triangular and trapezoidal threaded steel tie rods in assembly using finite element analysis. *Eng. Fail. Anal.* **2013**, *34*, 150–165. [\[CrossRef\]](#)
17. Duan, W.; Joshi, S. Failure analysis of threaded connections in large-scale steel tie rods. *Eng. Fail. Anal.* **2011**, *18*, 2008–2018. [\[CrossRef\]](#)
18. Kim, Y.; An, K.; Lee, K.; Park, Y. Structural Optimization of an Outer Tie Rod Using RSM and Kriging. *J. Korea Acad. Coop. Soc.* **2015**, *16*, 27–34. [\[CrossRef\]](#)
19. Waybase, P.S.; Takate, P.S.; Vaidya, R.; Patil, P.D. A Review on Weight Optimization of Tie Rod. *J. Emerg. Technol. Innov. Res.* **2019**, *6*, 155–156.
20. Godase, A.J.; Kulkarni, P.P.; Katekar, S. Probabilistic Design for Strength Analysis of Tie Rod Subjected to Tensile, Compressive, and Shear Load by Using Finite Element Methods. In *Techno-Societal 2018*; Springer: Pandharpur, India, 2020; pp. 109–119. [\[CrossRef\]](#)
21. Du, H.; He, Y.; Yang, Y.; Wang, Y. Study on tie rod force characteristics in electro-hydraulic power steering system for heavy vehicle. *Proc. Int. Mech. Eng. D J. Aut.* **2020**, *235*, 564–579. [\[CrossRef\]](#)
22. Muhammad, A.; Ali, M.; Shanono, I.H. Finite Element Analysis of a connecting rod in ANSYS: An overview. *IOP Conf. Ser. Mater. Sci. Eng.* **2020**, *736*, 022119. [\[CrossRef\]](#)
23. Bhirad, S.S. Failure Analysis and Optimization of the Tie Rod Using FEA. *Int. J. Res. Appl. Sci. Eng. Technol.* **2021**, *9*, 2781–2786. [\[CrossRef\]](#)
24. Kim, Y.; Park, S.; Lee, K.; Park, Y. Lightweight Design of an Outer Tie Rod Using Meta-Model Based Optimization Technique. *J. Korea Acad. Coop. Soc.* **2015**, *16*, 7754–7760. [\[CrossRef\]](#)
25. Navale, P.; Katekar, S.D. Validation of Natural Frequency for Tie Rod of a Steering System using Finite Element Analysis and Experimental Methods. *Int. J. Res. Appl. Sci. Eng. Technol.* **2023**, *11*, 139–154. [\[CrossRef\]](#)
26. Wayal, S.U.; Katratwar, T. Transient Dynamic Analysis for Optimization of Tie Rod Using FEM. *Int. J. Sci. Res. Publ.* **2016**, *6*, 263–267.

27. Zhang, Z.Y.; Shen, R.Y.; Wang, Q. The modal analysis of the liquid filled pipe system. *Acta Mech. Solida Sin.* **2001**, *22*, 143–149.
28. Jiao, Z.X.; Hua, Q.; Yu, K. Frequency domain analysis of vibrations in liquid filled piping systems. In Proceedings of the ASME 1999 International Mechanical Engineering Congress and Exposition. Fluid Power Systems and Technology, Nashville, TN, USA, 14–19 November 1999; pp. 25–31. [\[CrossRef\]](#)
29. Martucci, A.; Marchese, G.; Bassini, E.; Lombardi, M. Effects of Stress-Relieving Temperature on Residual Stresses, Microstructure and Mechanical Behaviour of Inconel 625 Processed by PBF-LB/M. *Metals* **2023**, *13*, 796. [\[CrossRef\]](#)
30. Tian, Z.; Zhang, C.; Wang, D.; Liu, W.Y.; Fang, X.; Wellmann, D.; Zhao, Y.; Tian, Y. A Review on Laser Powder Bed Fusion of Inconel 625 Nickel-Based Alloy. *Appl. Sci.* **2020**, *10*, 81. [\[CrossRef\]](#)
31. Anand Rao, K.S.; Gupta, R.K.; Ramchandran, P.; Rao, G.V. Non-linear static analysis of uniform slender functionally graded material beams using finite element method. *Proc. Natl. Acad. Sci. India Sect. A Phys. Sci.* **2011**, *81A*, 71–78. [\[CrossRef\]](#)
32. Sayatfar, A.; Khedmati, M.R.; Rigo, P. Residual ultimate strength of cracked steel unstiffened and stiffened plates under longitudinal compression. *Thin-Walled Struct.* **2014**, *84*, 378–392. [\[CrossRef\]](#)
33. Sayman, O.; Ozen, M.; Ozel, A.; Demir, T.; Korkmaz, B. A non-linear elastic-plastic stress analysis in a ductile double-lap joint. *Sci. Eng. Compos. Mater.* **2013**, *20*, 163–168. [\[CrossRef\]](#)
34. Mechel, F.P. Modal-analysis in curved and ring-shaped ducts. Part I: Curved Ducts. *Acta Acust. United Acust.* **2008**, *94*, 173–206. [\[CrossRef\]](#)
35. Mondal, R.N.; Huda, M.A.; Tarafder, D. Steady and unsteady solutions of the thermal flows through a curved duct. *Khulna Univ. Stud.* **2007**, *8*, 151–160. [\[CrossRef\]](#)
36. Hye, M.A.; Rahman, M.M. A Numerical Study on Non-Isothermal Flow Through a Rotating Curved Duct with Square Cross Section. *Int. J. Appl. Sci. Eng.* **2014**, *12*, 241–256.
37. Wahiduzzaman, M.; Alam, M.M.; Ferdows, M.; Sivasankaran, S. Non-isothermal flow through a rotating straight duct with wide range of rotational and pressure driven parameters. *Comp. Math. Math. Phys.* **2013**, *53*, 1571–1589. [\[CrossRef\]](#)
38. Ji, D.; Hu, X.; Zhao, Z.; Jia, X.M.; Hu, X.; Song, Y. Stress Rupture Life Prediction Method for Notched Specimens Based on Minimum Average von Mises Equivalent Stress. *Metals* **2022**, *12*, 68. [\[CrossRef\]](#)
39. Wang, S.; Wang, Y.; Yu, L.; Ji, K.; Liu, X.; Lou, Y. Failure Modeling for QP980 Steel by a Shear Ductile Fracture Criterion. *Metals* **2022**, *12*, 452. [\[CrossRef\]](#)
40. Choi, B.; Moon, I.Y.; Oh, Y.S.; Kang, S.; Kim, S.; Jung, J.; Kim, J.; Kim, D.; Lee, H.W. Die Design for Extrusion Process of Titanium Seamless Tube Using Finite Element Analysis. *Metals* **2021**, *11*, 1338. [\[CrossRef\]](#)
41. Živković, J.M.; Dunić, V.; Milovanović, V.; Pavlović, A.; Zivkovic, M.M. A Modified Phase-Field Damage Model for Metal Plasticity at Finite Strains: Numerical Development and Experimental Validation. *Metals* **2021**, *11*, 47. [\[CrossRef\]](#)
42. Li, H.; Wang, J.; Wang, J.; Hu, M.; Peng, Y. Lifetime Assessment for Multiaxial High-Cycle Fatigue Using Twin-Shear Unified Yield Criteria. *Metals* **2021**, *11*, 1178. [\[CrossRef\]](#)
43. Nieslony, A. A critical analysis of the Mises stress criterion used in frequency domain fatigue life prediction. *Frat. Integrita Strutt.* **2016**, *38*, 177–183. [\[CrossRef\]](#)
44. Lyu, Y.; Lian, W.; Sun, Z.; Li, W.; Duan, Z.H.; Chen, R.; Yu, W.; Shao, S. Failure Analysis of Abnormal Bulging and Cracking for High-Pressure Steam Pipe. *J. Mater. Eng. Perform.* **2022**, *31*, 7277–7289. [\[CrossRef\]](#)
45. Zhang, Y.; Du, Z.; Shi, L.; Liu, S.M. Determination of Contact Stiffness of Rod-Fastened Rotors Based on Modal Test and Finite Element Analysis. *J. Eng. Gas Turbines Power* **2010**, *132*, 094501. [\[CrossRef\]](#)

**Disclaimer/Publisher’s Note:** The statements, opinions and data contained in all publications are solely those of the individual author(s) and contributor(s) and not of MDPI and/or the editor(s). MDPI and/or the editor(s) disclaim responsibility for any injury to people or property resulting from any ideas, methods, instructions or products referred to in the content.